Article

Spatiotemporal Mapping and Monitoring of Whiting in the Semi-Enclosed Gulf Using Moderate Resolution Imaging Spectroradiometer (MODIS) Time Series Images and a Generic Ensemble Tree-Based Model

Abdallah Shanableh [1,2], Rami Al-Ruzouq [1,2,*], Mohamed Barakat A. Gibril [2], Cristina Flesia [3] and Saeed AL-Mansoori [4]

[1] Department of Civil and Environmental Engineering, University of Sharjah, Sharjah 27272, UAE; shanableh@sharjah.ac.ae
[2] Research Institute of Sciences and Engineering, University of Sharjah, Sharjah 27272, UAE; mbgibril@sharjah.ac.ae
[3] Department of Earth and Environmental Sciences, University of Milano Bicocca, Piazza Della Scienza 4, 20126 Milano, Italy; cristina.flesia@unimib.it
[4] Applications Development and Analysis Section (ADAS), Mohammed Bin Rashid Space Centre (MBRSC), Dubai 211833, UAE; Saeed.AlMansoori@mbrsc.ae
* Correspondence: ralruzouq@sharjah.ac.ae; Tel.: +971-6-505-0953

check for updates

Abstract: Whiting events in seas and lakes are a natural phenomenon caused by suspended calcium carbonate ($CaCO_3$) particles. The Arabian Gulf, which is a semi-enclosed sea, is prone to extensive whiting that covers tens of thousands of square kilometres. Despite the extent and frequency of whiting events in the Gulf, studies documenting the whiting phenomenon are lacking. Therefore, the primary objective of this study was to detect, map and document the spatial and temporal distributions of whiting events in the Gulf using daily images acquired by the Moderate Resolution Imaging Spectroradiometer (MODIS) on NASA's Terra and Aqua satellites from 2002 to 2018. A method integrating a geographic object-based image analysis, the correlation-based feature selection technique (CFS), the adaptive boosting decision tree (AdaBoost DT) and the rule-based classification were used in the study to detect, quantify and assess whiting events in the Gulf from the MODIS data. Firstly, a multiresolution segmentation was optimised using unsupervised quality measures. Secondly, a set of spectral bands and indices were investigated using the CFS to select the most relevant feature(s). Thirdly, a generic AdaBoost DT model and a rule-based classification were adopted to classify the MODIS time series data. Finally, the developed classification model was compared with various tree-based classifiers such as random forest, a single DT and gradient boosted DT. Results showed that both the combination of the mean of the green spectral band and the normalised difference index between the green and blue bands (NDGB), or the combination of the NDGB and the colour index for estimating the concentrations of calcium carbonates (CI) of the image objects, were the most significant features for detecting whiting. Moreover, the generic AdaBoost DT classification model outperformed the other tested tree-based classifiers with an overall accuracy of 97.86% and a kappa coefficient of 0.97. The whiting events during the study period (2002–2018) occurred exclusively during the winter season (November to March) and mostly in February. Geographically, the whiting events covered areas ranging from 12,000 km^2 to 60,000 km^2 and were mainly located along the southwest coast of the Gulf. The duration of most whiting events was 2 to 6 days, with some events extending as long as 8 to 11 days. The study documented the spatiotemporal distribution of whiting events in the Gulf from 2002 to 2018 and presented an effective tool for detecting and motoring whiting events.

---

1. Introduction

1.1. Background

Whiting is a short-lived phenomenon of milky parcels of water or bright in-water features, which has been reported globally in lacustrine, marine and freshwater environments and in semi-enclosed areas [1–7]. The ephemeral patches in whiting are turbid water with high levels of suspended fine-grained calcium carbonate mineral particles [8–11]. Whiting events last from days to weeks and can be visualised via satellite images as extended milky-white water varying from a few meters to square kilometres long [1,12].

Although whiting has been studied for decades to determine valid explanations for its occurrences and causes, the event remains controversial [10]. Various assumptions have been made to explain the causes of whiting. These assumptions include (1) the resuspension of fine-grained sediments caused by fish activities, microturbulent bursts and wind [8,12–15]; (2) bio-induced precipitation from the removal of CO_2 by photosynthesis [11,16–19] and (3) abiotic precipitation initiated by fluctuations in water temperature and ion activities related to climate change [8,20]. Carbonates, which are produced by the physical and biological disintegration of animal and algal bioclasts, blooms of microscopic algae during photosynthesis and abiotic precipitation or calcification of suspended picoplankton and organic matter, may be the possible sources of suspended carbonate minerals, such as aragonite and high and low magnesium calcite [8].

The occurrence of whiting has prompted researchers to establish a scientific description of the phenomena and to determine its association with climate change and oil deposition [21–23]. Whiting events are ephemeral, thus sample collection using traditional field measurements can be challenging, time consuming and costly. Remote sensing with ocean colour satellite instruments provides a set of high temporal-resolution data with various scales and records of satellite images and derivatives. This method enables the spatiotemporal mapping of whiting events; however, limited studies have adopted remote sensing technology to study these occurrences in marine environments [10]. The majority of the studies used satellite data to map whiting in the Bahama Banks [12,24], in the Ten Thousand Islands in southwest Florida [10,25], in the Great Lakes in North America [26] and in the Feldberg Lake District, Klocksin Lake Chain and Rheinsberg Lake regions in Germany [27]. Whiting events based on general properties are varyingly recognised with remote sensing data from visual identification and manual delineation [10,24,28–31]. Dierssen et al. [12] studied the spectral behaviour of whiting to identify the spatial extent of whiting patches in the Bahama Banks. Considering the shallowness of the southwest Florida coast and the spectral similarity between whiting occurrences and bright shallow bottom sediments, Long et al. [25] delineated whiting patches manually by relying on visual inspection and spatial contrast. Recently, Long et al. [10] used contrast enhancement and floating algae index (FAI) images to differentiate in-water whiting features from clouds to map the spatiotemporal variability of the southwest Florida whiting events from 2003 to 2015. Other studies focused on detecting and estimating the concentration of particulate inorganic carbon (PIC), or calcium carbonate particles, in the surface layer of the water column from the water-leaving radiance and reflectance differences concept through the computation of chlorophyll-a concentration [32–34].

The whiting phenomenon in the Gulf was initially reported in the 1960s. In 1962, Wells and Illing [35] observed whiting in numerous places in the Gulf such as in the eastern part of the Qatar Peninsula towards the coast of Abu Dhabi and off the coast of Saudi Arabia between Ras Tanura and Ras Safaniya. Although more than 50 years have passed since whiting events were initially reported in the Gulf, this phenomenon remains unclear [36,37]. To the best of the authors' knowledge, limited

effort has been exerted to map whiting in the Gulf using remote sensing techniques. The objectives of the present study were: (1) to adopt the correlation-based feature selection (CFS) to identify the most significant features for whiting extraction, (2) to develop a semi-automated framework to detect the whiting coverage in the Gulf from the Moderate Resolution Imaging Spectroradiometer (MODIS) images, using adaptive boosting (AdaBoost) and rule-based classification approach, (3) to compare and assess the performance of various applied tree-based machine learning methods, namely, the single decision tree (DT), random forest and the gradient boosted decision tree (GBDT)and (4) to document the frequency, duration, seasonality, spatial coverage and distribution of whiting occurrences in the Gulf between 2002 and 2018 using satellite observations.

1.2. Study Region

The Arabian Gulf is located in the Middle East and surrounded by the coasts of eight countries, namely, United Arab Emirates (UAE), Saudi Arabia, Oman, Kuwait, Bahrain, Iraq, Qatar and Iran (Figure 1). The Gulf is a semi-enclosed marginal sea positioned in a subtropical hyperarid region (between the latitudes of 24° to 30°N and the latitudes of 48° to 57 °E), with an average annual rainfall of less than 5 cm in the coastal areas [33,34]. The Gulf is nearly 990 km long and 56–370 km wide. It has an average depth of 36 m and a maximum depth of nearly 100 m and occupies a surface area of 239 km^2. The deepest region of the Gulf (more than 40 m deep) is near the Iranian coast and continues into the Strait of Hormuz. Meanwhile, the shallowest regions (less than 20 m deep) are located along the coasts of the UAE, Qatar, Bahrain and around the head of the Gulf. Owing to its shallowness, sea surface temperatures fluctuate significantly and the Gulf is considered as the hottest sea in the world during summer [35,38]. The seawater temperature ranges from less than 20 °C in winter to over 34 °C in summer. As a result of high evaporation rates during the hot and long summers in the region and the lack of precipitation, water in the Gulf is characterised by high salinity greater than 39 psu [33,39,40]. The Gulf is subjected to strong winds and often associated with dust storms, with the most extreme occurring in summer and late spring and moderate dust storms occurring in winter.
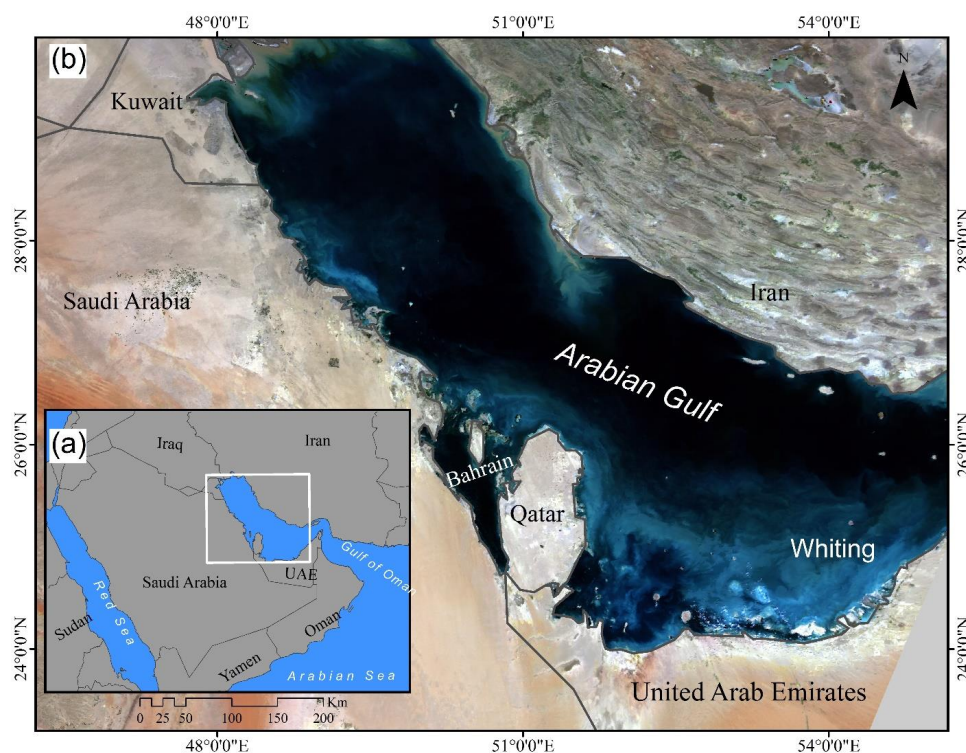

Figure 1. Map of the Gulf; (**a**) location map and (**b**) Moderate resolution imaging spectroradiometer (MODIS) satellite image with true colour captured on 1 March 2003 showing milky patches.

2. Methodology

2.1. Overview

Daily satellite data from MODIS for the period of 2002 to 2018 were obtained and visually inspected for whiting. The dates of whiting events were then classified in accordance with the month of the occurrence and the number of consecutive days during which whiting persisted. The data were then used to analyse frequency, seasonality and duration of whiting events in the Gulf.

The identification, mapping and classification of whiting in the Gulf required the extensive analysis of the acquired MODIS data. The analysis framework, which is illustrated in Figure 2, is summarised as follows: (1) preprocessing of the MODIS satellite data, (2) multiresolution image segmentation and parameter optimisation, (3) selection of the significant attributes using CFS, (4) classification of the daily MODIS time series images using AdaBoost DT and rule-based classification and (5) identification of the whiting spatiotemporal pattern (time series frequency, duration and seasonality, spatial coverage and distribution) in the Gulf. The aforementioned steps are further discussed in the following subsections.
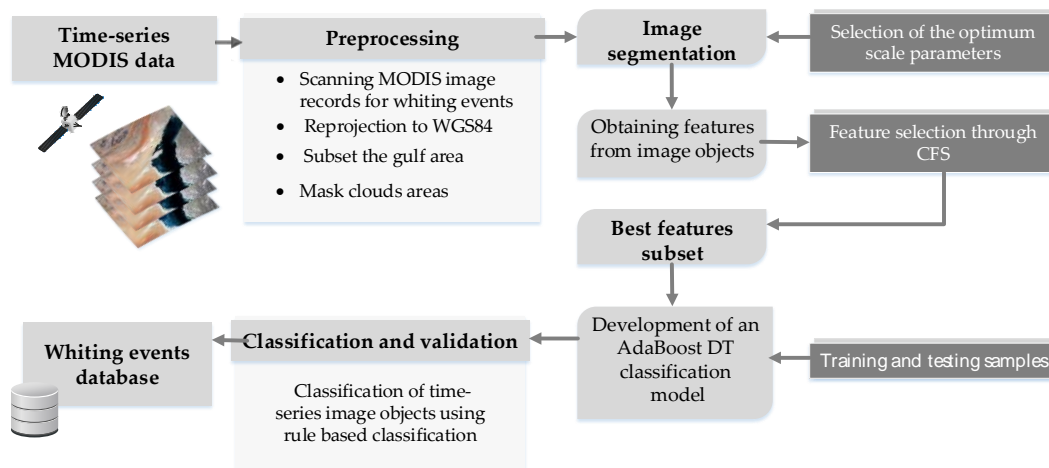
**Figure 2.** Flowchart of the overall procedure.

2.2. MODIS Datasets for Whiting Exploration

The exploration of whiting events in the Gulf as a short-lived, repetitive phenomenon by field-based studies is challenging. Therefore, high temporal resolution satellite images offered excellent sources of data for mapping and monitoring whiting in the Gulf. The daily high temporal-resolution Terra/Aqua MODIS surface reflectance products (MOD09GA and MYD09GA) with a coarse spatial resolution of 500 m were used in this study. The products, which covered the entire Gulf in one scene for the period of 2002–2018, were downloaded from NASA's Earthdata website (https://search.earthdata.nasa.gov/search). These products were atmospherically corrected by the MODIS Land Science Team for aerosols, thin cirrus clouds and gases.

Figure 3 illustrates the initiation and disappearance of a whiting event from February to March 2003. The consecutive MODIS images show the dramatic changes during the 6 consecutive days of observation. High-resolution satellite images, such as from the Landsat, with a 30 m spatial resolution and 16-day temporal resolutions, or from the Sentinel-2, with a 5-day revisit time and 10 m resolution, may be insufficient to capture such short-term whiting events given their limited temporal resolution.

The MODIS products (MOD09GA and MYD09GA) contained seven spectral bands with a spatial resolution of 0.5 km. Their reflectance bands were band 1 (red: 0.620–0.670 μm), band 2 (near infrared (NIR): 0.841–0.876 μm), band 3 (blue: 0.459–0.479 μm), band 4 (green: 0.545–0.565 μm), band 5 (shortwave infrared (SWIR1): 230–1.250 μm), band 6 (shortwave infrared (SWIR2): 1.628–1.652 μm) and band 7 (shortwave infrared (SWIR3): 2.105–2.155 μm). The data were reprojected from the sinusoidal coordinate system to the World Geodetic System 1984 and then converted from heirarchical

data format to georeferenced tagged image file format. The images were then cropped on the basis of the boundaries of the Gulf.
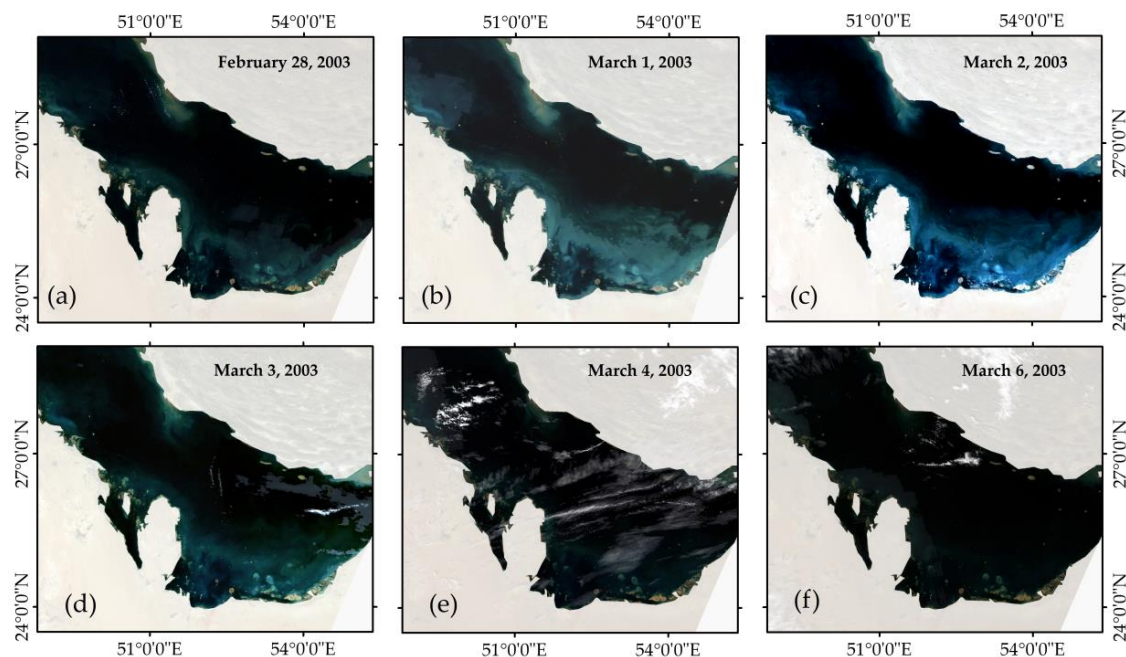
Figure 3. Initiation and disappearance of a whiting event in 2003 based on acquired MODIS images.

The whiting events appeared in the MODIS satellite images as turbid and milky features. The spectral response of various surface water features at different locations in the Gulf appeared in a sample MOD09GA product during a whiting event and shown in Figure 4a–h. Figure 4f–h show whiting events with high intensities of bands 3 (blue region of the spectra) and 4 (green region of the spectra). Figure 4e shows a clear water sample with a low intensities of all bands. Shallow areas at the northwest section of the gulf show high reflections in bands 1 (red region of the spectra) and 2 (NIR region of the spectra), as shown in Figure 4a. Overall, the images show variations in terms of relative intensities of bands 3 and 4 and bands 1 and 2. Meanwhile, the intensities of bands 5, 6 and 7 did not exhibit significant variations.

2.3. Object-Based Analysis and Image Segmentation Optimisation

A traditional per-pixel classification approach is useful for feature extraction when the targets of interest are smaller than the spatial resolution of the remotely sensed data [41]. This approach only considers the spectral properties of each pixel and disregards any spatial or contextual information related to the classified pixel [42]. Geographic object-based image analysis (GEOBIA) has been extensively used in classifying very-high spatial resolution data as an alternative to a pixel-based approach. GEOBIA works by assessing spatially neighbouring groups of pixels rather than individual pixels [43]. GEOBIA is not only limited to high resolution images because the approach is not spatial-resolution dependent; therefore, it can be applied to different resolutions if the sizes of the intended objects are compatible with the spatial resolution of the images [44,45]. Thus, GEOBIA has been successfully adopted and implemented to classify MODIS time series data in different applications [44–50].

The generic GEOBIA framework can be divided into (1) image segmentation, which is the process of generating homogenous and nonoverlapping image objects/segments from image pixels and (2) image object/segments classification [51]. The multiresolution image segmentation algorithm (MRS) [52], which is one of the most used algorithms, is applied to the time series MODIS data. The MRS is a bottom-up region-growing algorithm that commences with pixels as individual segments.

MRS is govened by three main parameters, namely, (a) scale, (b) shape/color weight and (c) compactness/smoothness weight. This algorithm merges neighbouring pixels in each successive step on the basis of homogeneity (shape and compactness), which describes the similarity of contiguous objects. The degree of fitting, which is a value determined by the scale parameter defined by an analyst, is measured in each merging procedure. Moreover, the merge is performed if the degree of fitting is less than the minimum degree of fitting [53]. The scale parameter is one of the most critical parameters in the segmentation process. It profoundly influences resultant image objects and subsequent classification steps because it controls the size of image-generated objects [54,55]. Selecting high-scale values generate large image objects (undersegmentation), whereas selecting small-scale values yield small image objects (oversegmentation). Thus, the utilisation of an optimisation technique to find the optimum scale parameters for delineating whiting is vital to avoid the subjectivity of using a trial and error visual approach.
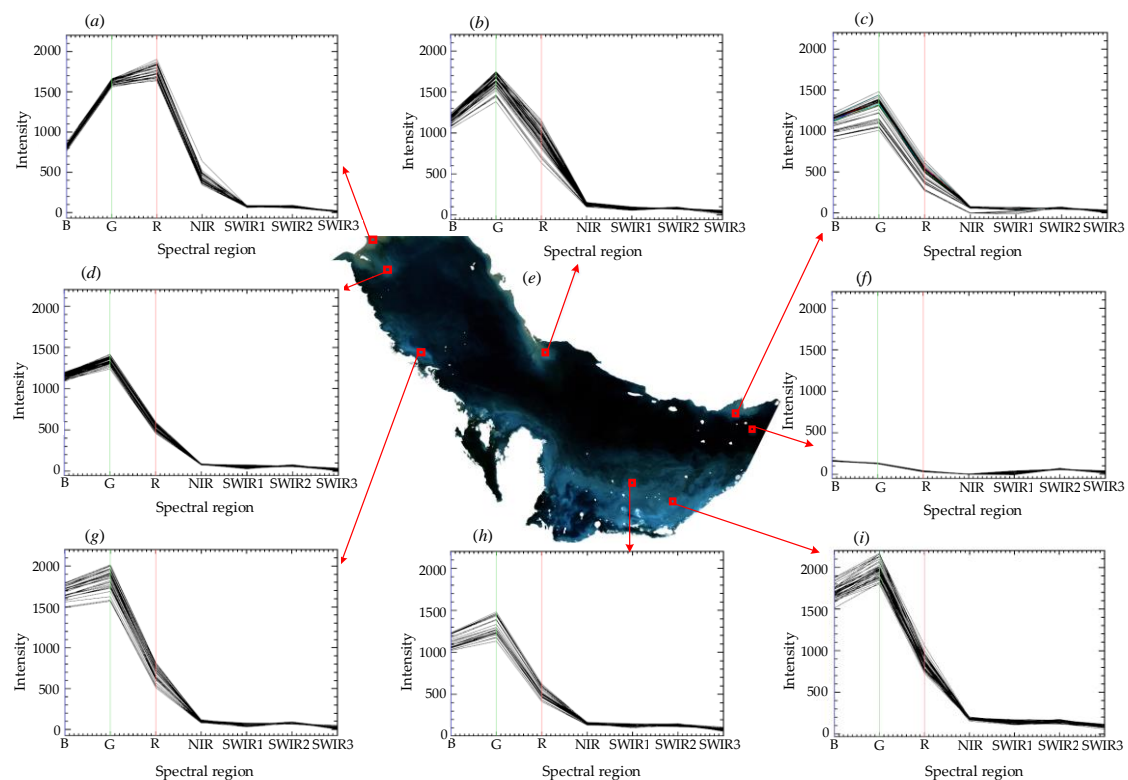
Figure 4. Spectral response of various surface features in a sample MODIS product (MOD09GA) for the Gulf.

Several unsupervised segmentation quality measures have been utilised in the literature to identify the best scale parameters [56–59]. In the current study, the performance of two unsupervised segmentation quality measures, namely, the objective function (OF) [60] and the F-measure [57] were compared to find an optimum scale value that accurately delineates whiting. Both measures adopt oversegmentation and undersegmentation metrics by using the values of weighted variance and spatial autocorrelations (Moran's I). They are expressed in Equations (1)–(5).

$$OF = WV_{norm} + MI_{norm}, \tag{1}$$

$$F - measure = 2 * \frac{MI_{norm} \times WV_{norm}}{MI_{norm} + WV_{norm}}, \tag{2}$$

$$WV = \frac{\sum_{i=1}^{n} a_i . v_i}{\sum_{i=1}^{n} a_i}, \tag{3}$$

$$\text{MI} = \frac{n \sum_{i=1}^{n} \sum_{j=1}^{n} w_{i,j}(z_i - \overline{z})(z_j - \overline{z})}{\left(\sum_{i=1}^{n} (z_i - \overline{z})^2\right) \left(\sum_{i \neq j} \sum w_{i,j}\right)}, \tag{4}$$

where MI_{norm} and WV_{norm} are the normalised Moran's I and weighted variance, respectively. In Equation (3), WV denotes the weighted variance and a_i and v_i are the area and variance of image object/segment (generated by MRS) i, respectively. In Equation (4), n symbolises the total number of objects, z_i and z_j are the means of the spectral value of image objects i (Oi) and j (Oj), respectively, $\overline{z}$ is the mean spectral value of the total objects in a specific band and $w_{i,j}$ is a spatial proximity measure between image objects i (Oi) and j (Oj) in which nearby image objects are defined as 1 and other objects are considered as 0. The normalised function for WV and MI can be expressed using the following equation

$$F(X) = \frac{X_{max} \cdot X}{X_{max} \cdot X_{min}}, \tag{5}$$

where X, X_{max} and X_{min} are the original, maximum and minimum values of the weighted variance or Moran's I for a spectral band, respectively. The highest values of the OF or F-measure indicate high segmentation quality and the optimum scale is identified as the scale that achieves image objects with the highest OF or F-measure values. After the selection of an appropriate scale to delineate whiting, various spectral features and indices were computed and investigated to find the most relevant features to be used in the classification phase.

2.4. Feature Selection

One of the strongest characteristics of GEOBIA is it enables the generation of hundreds of features or attributes for analysis (e.g., spectral bands and indices, textural, geometric and contextual attributes). The extraction and utilisation of a considerable number of features (e.g., variables or attributes) in the analysis are computationally intensive; hence, they can negatively affect classification accuracy [61]. Therefore, FS, which involves the selection of an essential feature subset from an enormous amount of generated features, is a decisive step used in image analysis procedures. In addition, FS can achieve an equivalent or higher classification accuracy than the original feature space and improve the efficiency of GEOBIA [62–66]. FS methods may be generally grouped into three classes, namely, filter, wrapper and embedded methods [64,65]. The filter method is considered the simplest and fastest method among the three classes. It utilises certain statistical measures (e.g., correlation coefficients, variance, chi-square test measures and ANOVA F-values) to rank and select relevant features without using any learning algorithms [64,67–69]. By contrast, the wrapper method adopts a classification algorithm as part of the evaluation process to classify the training data and assess the results. The wrapper method selects the most significant feature subset that produces the highest classification accuracy [70,71]. Finally, the embedded method exhibits a trade-off between the filter and the wrapper methods. This method is considered feature ranking because features are selected during the construction of a classification model without further evaluating the selected feature subset [65]. Comparisons of various FS techniques are available in the literature [64,72–74].

A wrapper method that combines CFS and the naïve Bayes classifier was used in this study to find the most relevant features for extracting whiting features. CFS has recently been successfully applied to FS and has outperformed various FS techniques with GEOBIA [63,75].

2.4.1. CFS

CFS is a popular approach that uses a search algorithm with a heuristic evaluation function to assess the merit of feature subsets [76,77]. It measures the worth of each feature to predict the class label along with the intercorrelation level among features [78]. A heuristic evaluation function is designed on the basis of the hypothesis that superior feature subsets encompass correlated features

with classes though they remain uncorrelated with one another [76,79]. Merits (heuristics) can be formalised using the following formula

$$\text{Merits} = \frac{k\bar{r}_{cf}}{\sqrt{k + k(k-1)\bar{r}_{ff}}},\tag{6}$$

where k denotes the number of features, f indicates the feature, $\bar{r}_{cf}$ symbolises the mean feature correlation with a class and $\bar{r}_{ff}$ is the average intercorrelation among subset features.

2.4.2. Feature Acquisition and Computation

In general, various spectral indices and bands may be used to map water surface features and water bodies. In this study, numerous attributes, such as mean spectral reflectance, standard deviation and spectral indices, which have been previously reported in the literature, were computed for the image objects of several images for FS. Table 1 lists the 32 attributes that were examined using CFS.

Table 1. Description of the examined features derived from MODIS images.

No.	Examined Feature Name	Abbreviations	Description	MODIS Bands	Ref.
1–7	Mean values of an image object of MODIS reflectance (ref.) bands	Ref. 1–7	Mean of bands 1–7 (Red, NIR, Blue, Green, SWIR1, SWIR2 and SWIR3)	B1–B7	[80]
8–14	Standard deviation of an image object of ref. bands	SD 1–7	Standard deviations of individual bands 1–7	B1–B7	[80]
15	Normalised difference vegetation index	NDVI	$\frac{(\text{Ref.}_{NIR}-\text{Ref.}_{Red})}{(\text{Ref.}_{NIR}+\text{Ref.}_{Red})}$	B2, B1	[81]
16	Normalised difference water index	NDWI	$\frac{(\text{Ref.}_{Green}-\text{Ref.}_{NIR})}{(\text{Ref.}_{Green}+\text{Ref.}_{NIR})}$	B4, B2	[82]
17	Modified normalised difference water index	MNDWI	$\frac{(\text{Ref.}_{Green}-\text{Ref.}_{SWIR1})}{(\text{Ref.}_{Green}+\text{Ref.}_{SWIR1})}$	B4, B7	[83]
18	Floating algae index	FAI	$\text{Ref}_{NIR}-[\text{Ref.}_{Red}+(\text{Ref.}_{SWIR1}-\text{Ref.}_{Red})*\frac{(859-645)}{(1240-645)}]$	B1, B2, B5	[84]
19	Color index for estimating PIC	CI	$\text{Ref.}_{Green}-[\text{Ref.}_{blue}+(\text{Ref.}_{Red}-\text{Ref.}_{Blue})*\frac{(555-443)}{(670-443)}]$	B1, B3, B4	[85]
20	Color index using 547, 667 and 869 nm for estimating PIC	CI869	$\text{Ref.}_{Red}-[\text{Ref.}_{Green}+(\text{Ref.}_{NIR}-\text{Ref.}_{Green})*\frac{(667-547)}{(869-547)}]$	B1, B2, B4	[34]
21	Color index using 547 and 667 nm for estimating PIC	CI2	$\text{Ref.}_{Green}-\text{Ref.}_{Red}$	B1, B4	[34]
22	Normalised difference algal bloom index	NDBI	$\frac{(\text{Ref.}_{Green}-\text{Ref.}_{Red})}{(\text{Ref.}_{Green}+\text{Ref.}_{Red})}$	B4, B1	[86]
23	Shortwave infrared water stress index	SIWS	$\frac{(\text{Ref.}_{SWIR2}-\text{Ref.}_{NIR})}{(\text{Ref.}_{SWIR2}+\text{Ref.}_{NIR})}$	B6, B2	[87]
24	Ratio vegetation index 1	RVI 1	$\frac{\text{Ref.}_{NIR}}{\text{Ref.}_{Red}}$	B2, B1	[88]
25	Ratio vegetation index 2	RVI 2	$\frac{\text{Ref.}_{Red}}{\text{Ref.}_{NIR}}$	B1, B2	[88]
26	Enhanced vegetation index	EVI	$2.5\frac{(\text{Ref.}_{NIR}-\text{Ref.}_{Red})}{1+\text{Ref.}_{NIR}+6\text{Ref.}_{Red}-7.5\text{Ref.}_{Blue}}$	B2, B1, B3	[89]
27	Ratio of the reflectance values of red and green bands	Ratio RG	$\frac{(\text{Ref.}_{Red}-\text{Ref.}_{Green})}{(\text{Ref.}_{Red}+\text{Ref.}_{Green})}$	B1, B4	[90]
28	Blue/red index	BRI	$\frac{\text{Ref.}_{Blue}}{\text{Ref.}_{Red}}$	B3, B1	[91]
29	Blue/green index	BGI	$\frac{\text{Ref.}_{Blue}}{\text{Ref.}_{Green}}$	B3, B4	[91]
30	Normalised difference between green and red bands	NDGR	$\frac{(\text{Ref.}_{Green}-\text{Ref.}_{Red})}{(\text{Ref.}_{Green}+\text{Ref.}_{Red})}$	B4, B1	-
31	Normalised difference between green and blue bands	NDGB	$\frac{(\text{Ref.}_{Green}-\text{Ref.}_{Blue})}{(\text{Ref.}_{Green}+\text{Ref.}_{Blue})}$	B4, B3	-
32	Normalised difference between blue and green bands	NDBG	$\frac{(\text{Ref.}_{Blue}-\text{Ref.}_{Green})}{(\text{Ref.}_{Blue}+\text{Ref.}_{Green})}$	B3, B4	-

The present study used CFS and the naïve Bayes classifier to determine the most relevant feature subset for extracting whiting events from the multitemporal MODIS data. Then, training and testing samples were prepared from the image objects of various whiting events. Table 2 shows the dates and number of samples that were selected for FS. These samples were normalised to a scale from 0 to 1 and then split 70% for training and 30% for testing.

Table 2. Dates and number of image object samples selected from various images.

Dates	Whiting Samples	Clear Water	Other Segments
28 February 2003	74	149	74
2 March 2003	100	125	126
3 March 2003	121	36	74
26 February 2004	69	124	66
2 February 2018	36	160	72
Sum	400	594	412

The optimised image objects with the selected significant features via CFS were ultimately used to classify whiting using various tree-based classification algorithms.

2.5. Boosting Decision Tree Classification

Boosting is an ensemble machine learning algorithm that is used to improve the accuracy of a classifier by decreasing the classification algorithm's sensitivity to noise and labelling errors in the training datasets [92,93]. The performance of numerous classifiers (weak learners) that are learned by resampled versions of the training samples is combined to improve classification accuracy. Boosting DTs are ensemble methods that use multiple iterations of DT classifiers. A boosted DT called the AdaBoost algorithm was adopted in this study.

AdaBoost [92], also known as adaptive boosting, is a generic iterative supervised learning algorithm that combines multiple classifiers (weak classifiers) to obtain high accuracy. The AdaBoost algorithm chooses training samples on the basis of adaptive resampling by selecting misclassified datasets produced by a previous classifier. The erroneously classified samples in a prior iteration are selected more often than correctly classified samples. Furthermore, new DT models are forced to focus on the misclassified samples and minimise the errors of the former trees [94,95]. Misclassified training samples are given increased weights in each iteration; thus, the classifier can improve its performance in new datasets. Ultimately, all trees (not only a final tree or trees) are incorporated because the additive model is designed such that combinations of all trees can give the optimum solution [96].

Given surface water features with diverse spectral values, training image objects were selected to represent five classes with different spectral responses, namely, whiting, low whiting, clear water, interlayer (a class with subtle differences between low whiting and clear water), apparent sediment (shallow areas next to the shore) and apparent green (potential true green-coloured algae). The prepared samples with the most significant features selected by CFS were split 70% for training and 30% for assessing the performance of the AdaBoost classification model. Using the verified prediction model developed by the AdaBoost algorithm, the multitemporal image objects were classified into the aforementioned five classes by rule-based classification. The performance of the AdaBoost classification technique was compared with that of various tree-based classification algorithms, such as random forest, the single DT and the gradient boosted decision tree. Classification results were assessed in this study by computing the overall accuracy (OA), the Kappa coefficient (KC) from the confusion matrix. While the OA of the classification indicates the percentage of correctly classified image objects, the KC statistically measures and analyses the degree of agreement between the classified and reference image objects [97].

3. Results & Discussion

The results of the spatiotemporal mapping of whiting in the Gulf using the MODIS time series images and a generic ensemble tree-based model are presented in this section. Furthermore, the frequency, seasonality, duration and geographic distribution and extent of whiting events in the Gulf are also documented and analysed.

3.1. Whiting Temporal Pattern in the Gulf

The primary objective of this study was to map the spatial and temporal extents of whiting in the Gulf for 16 years by using satellite images. Therefore, a total of 5800 image scenes of the Gulf were inspected prior to the analysis to detect the existence of whiting. Cloud-free image sets obtained for the period of 2002 to 2018 were used to generate generic statistics on the seasonality, frequency and duration of whiting events in the Gulf, as shown in Table 3.

Table 3. Statistics of occurrence of whiting in the Gulf for 16 years (July 2002 to July 2018).

Year	Month	Dates	Period (d)	Frequency Event	Year	Month	Dates	Period (d)	Frequency Event
2002	February	1–5	5	1		November	10–11	2	2
	December	23–30	8	1		November	24–25	2	
2003	February	28–1	2	-		December	1–6	6	2
	March	1–3	3	1		December	27–30	4	
	December	9–11	3	1		January	15–16	2	2
2004	January	29–31	3	1		January	21–26	6	
	February	7–10	4			February	3–7	5	2
	February	16–17	2	3	2012	February	21–24	4	
	February	25–27	3			March	4–13	10	2
	March	21–23	3	1		March	18–19	2	
	November	24–29	6	1		November	2–3	2	2
2005	February	10–11	2	1		November	12–14	3	
	November	1–11	11	2		January	11–18	8	1
	November	24–31	8			February	4–5	2	2
2006	January	15–20	6	1	2013	February	14–15	2	
	December	9–10	2	2		March	12–13	2	1
	December	25–26	2			December	11–18	8	2
2007	January	1–4	4	1		December	20–27	8	
	March	4–5	2	2		February	11–13	3	2
	March	11–13	3			February	19–21	3	
	April	19–21	3	1	2014	November	7–10	4	2
	November	25–30	6	1		November	26–30	5	
	December	11–13	3	2		December	2–7	6	2
	December	24–25	2			December	25–26	2	
2008	February	3–7	5	2		January	19–24	6	1
	February	21–27	7		2015	February	27–28	2	1
	March	6–7	2	1		November	13–15	3	1
	December	17–19	3	1		Jan	4–6	3	1
2009	January	4–7	4	2	2016	Jan–Feb	29–2	4	1
	January	14–16	3			February	10–13	4	1
	February	3–6	4	1		February	4–8	5	1
	November	7–8	2	1	2017	November	10–14	5	2
2010	January	27–28	2	1		November	29–30	2	
	November	23–28	6	1		December	4–5	2	1
	December	16–17	2	1		January	2–5	4	1
2011	January	12–14	3	1	2018	January	29–31	3	1
	February	4–5	2	2		February	1–4	4	1

The results showed that whiting events reoccurred in the region exclusively during the winter season (November to March). Figure 5 enumerates the number of events per month/year and the number of days per month/year where whiting events occurred during the study period (2002–2018). The frequency of whiting events during the study period ranged from one to two events per winter month to two to eight events per year. The highest frequency of whiting events was observed in February. The total number of whiting days ranged from 2 to 11 days per month to 8 to 34 days per year. Furthermore, the duration of individual events ranged from 2 to 8 days. The total number whiting days during the past 16 years was approximately 289 days or approximately 7% of the total number of days or 16% of the total days (November to March).
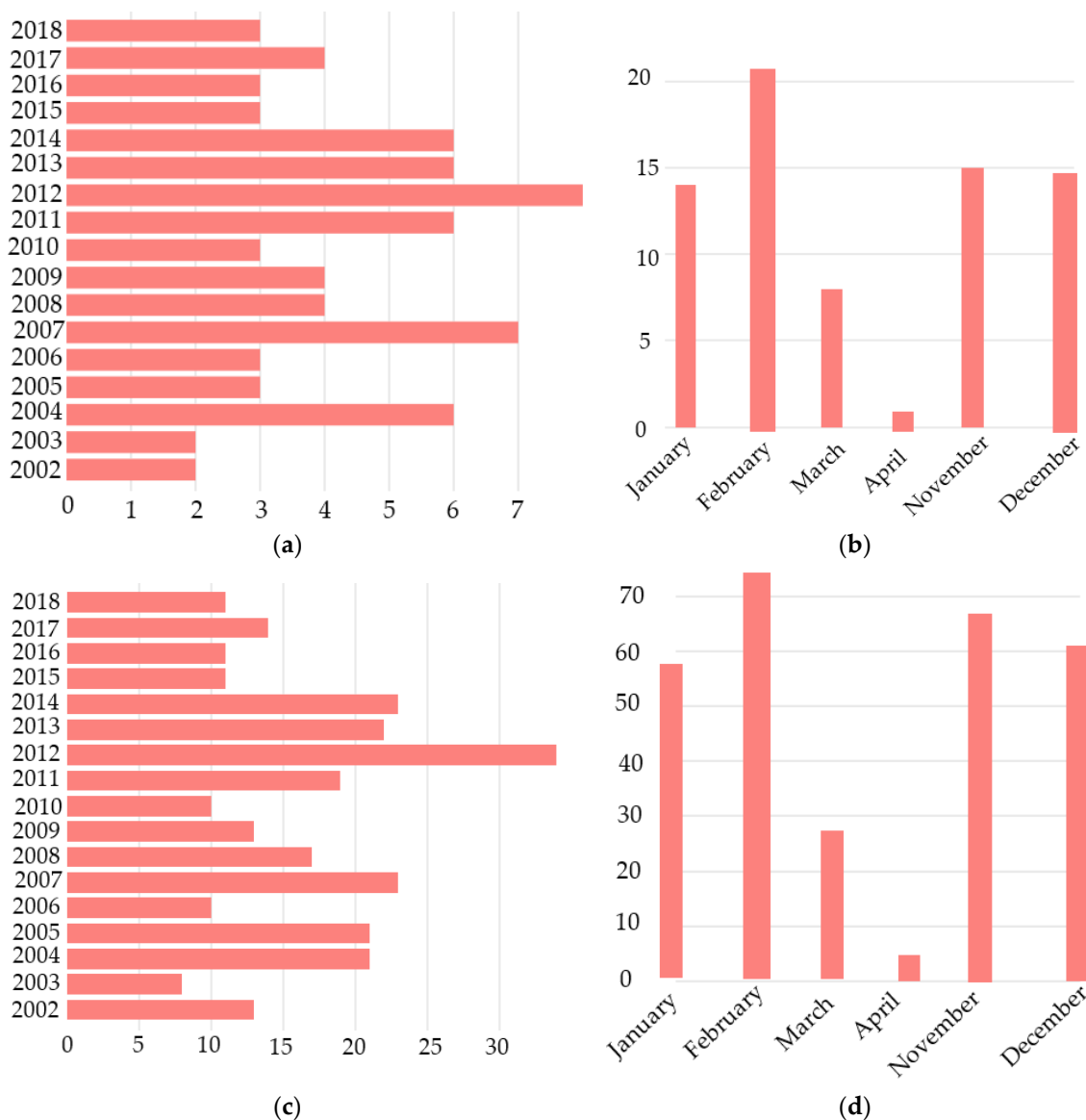
Figure 5. Generic statistics of whiting occurrence: (**a**) total frequency per year, (**b**) total frequency per month, (**c**) total number of days per year and (**d**) total number of days per month.

3.2. Results of the Integrated GEOBIA Approach

3.2.1. Results of Image Segmentation

Unsupervised image segmentation quality measures based on the OF and the F-measure were utilised to find the optimal scale for whiting event delineation by varying the scale parameter. The mean values of NIR image objects are frequently used in image segmentation assessments to compute undersegmentation and oversegmentation metrics. However, the NIR reflectance band was unsuitable for assessing the segmentation of images with whiting occurrences because the whiting phenomenon does not exist on this band. Therefore, the mean values and standard deviation of the mean blue spectral image objects were used to compute the OF and the F-score values (Equations (1)–(5)). Table 4 provides a sample of the OF and the F-measure computations for a single image acquired on 2 March 2003. The highest OF and F-measure values were on a scale value of 40. Thus, scale 40 was selected as the optimum scale value. The values of the shape and compactness parameters were set as 0.5 and 0.1, respectively.

Table 4. Optimum scale parameter values selected for a single scale using the objective function (OF) and the F-measure methods (Equations (1)–(2)).

SP	No. of Objects	Weighted Variance	Moran's I	WV Norm	MI Norm	OF	F-Measure
10	32,227	326.8510	0.4118	1	0	1	0
20	12,446	1012.3473	0.2597	0.8883	0.3747	1.2630	0.5271
30	6695	1784.3010	0.2013	0.7625	0.5187	1.2812	0.6174
40	4208	2606.2537	0.1425	0.6285	0.6636	1.2921	0.6456
50	2891	3394.2522	0.1022	0.5001	0.7630	1.2631	0.6042
60	2197	4173.2623	0.0789	0.3732	0.8204	1.1936	0.5130
70	1755	4780.7261	0.0485	0.2742	0.8953	1.1695	0.4198
80	1459	5468.1106	0.0316	0.1621	0.9370	1.0991	0.2764
90	1202	6039.1318	0.0178	0.0691	0.9708	1.0399	0.1290
100	1039	6463.0462	0.0060	0	1	1	0

3.2.2. Results of FS and Analysis

FS reduces the dimensionality of data, diminishes the complexity of classification models, minimises overfitting and accelerates the process. CFS was selected among various FS methods because of its successful implementation in several remote sensing applications. As listed in Table 1, various spectral bands and indices were examined to determine the most significant features for detecting whiting event occurrences from a large number of MODIS images. Given the considerable variation between the examined features in terms of range and numerical value, all the data were normalised to a scale ranging from 0 to 1. The CFS algorithm with the best-first search strategy [98] was implemented along with the naïve Bayes classifier to evaluate the worth of the selected features. Accuracy was assessed via tenfold stratified cross-validation on the selected training data. According to the results, the best-first eight significant features were the green (G), NDGB, FAI, CI, CI2, CI869, BRI and SD-R. Therefore, combinations of each pair of the best-first selected features were selected for further examination. Figure 6 shows the possible combinations of the selected features and their corresponding overall accuracy and kappa coefficient. These tests reveal that the utilisation of the NDGB and the mean green attribute values or the NDGB and CI of the image objects were similarly excellent features for accurately mapping whiting using the MODIS data. This finding was typically consistent with the spectral analysis of various surface features shown in Figure 4. In this study, the NDGB and the green band were selected for further analysis.

3.2.3. Classification Results

Given the lack of historical records of whiting events in the Gulf, the AdaBoost model was trained and tested with samples selected on the basis of satellite image inspection and the recommendation of Wells and Illing (1962). Figure 7 depicts the generated AdaBoost DT model from the most significant features, namely, the mean green and the NDGB, to extract whiting event features from satellite images with moderate spatial resolution. Optimised time series image objects were eventually classified into six classes (namely, clear water, interlayer, low whiting, whiting, apparent green and apparent sediments) by the developed AdaBoost model and GEOBIA rule-based classification. Whiting water with a high intensity can be simply identified with the generic developed model by rule-based classification when the slope (NDGB) is less than 0.1 and the intensity of the green band is greater than 1500 in the MODIS scene. Whiting with a low intensity can be recognised when the slope (NDGB) is less than 0.1 and the mean of the green band range is between 750–1500.
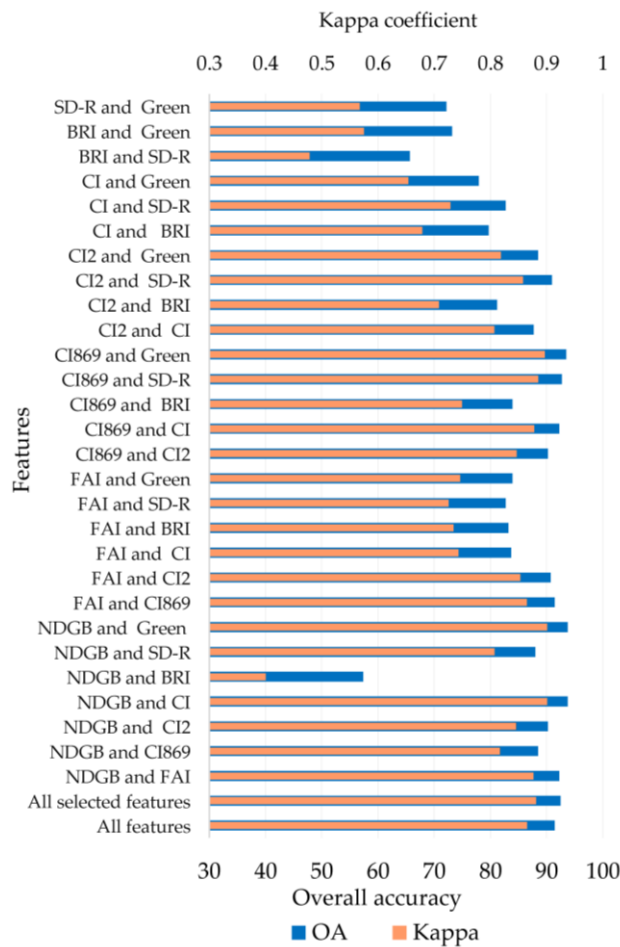
Figure 6. Performance of the combinations of multiple selected features.
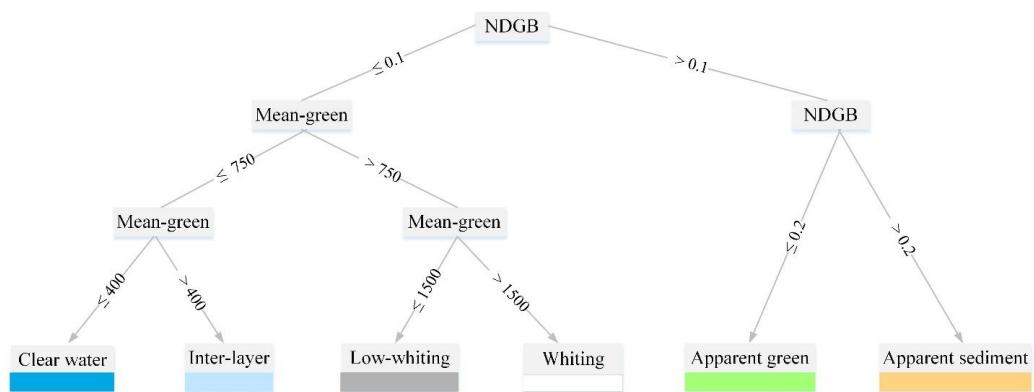

Figure 7. AdaBoost DT-generated model for developing rule sets for rule-based classification.

Figure 8a–h present four classification results together with the original images acquired on 2 March 2003, 4 March 2012, 10 February 2016 and 3 October 2018. Figure 8a–d show extensive whiting along the coasts of UAE and Qatar, whereas Figure 8e,f show low levels of whiting. As expected from the classification model, Figure 8g,h represent clear water without any significant whiting.
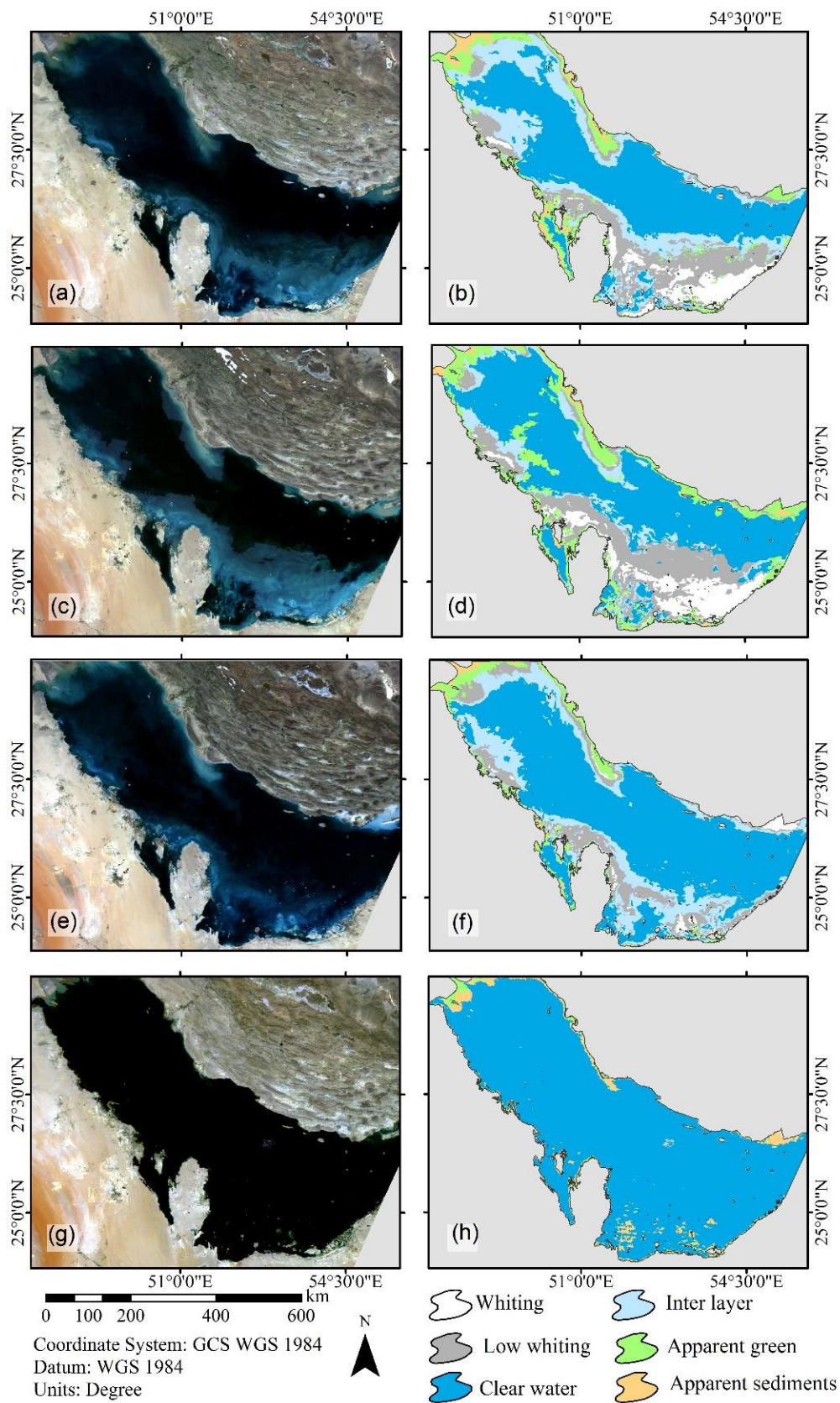
Figure 8. MODIS images and their classification results: (**a**,**b**) 2 March 2003, (**c**,**d**) 4 March 2012, (**e**,**f**) 10 February 2016 and (**g**,**h**) 3 October 2018.

The performance of the developed AdaBoost classification model was compared with that of the three tree-based classification algorithms. The AdaBoost classification model gave superior classification outcomes compared to the other models, as shown in Table 5.

Table 5. Accuracy assessment of various tree-based classifiers.

Classifier	OA	KC
AdaBoost DT	97.86%	0.97
Gradient boosted DT	97.12%	0.96
Single DT	96.19%	0.95
Random forest	95.00%	0.93

3.3. Spatial Distribution of Whiting in the Gulf

Generalisation of the occurrence pattern of whiting in the Gulf can be challenging because of the existence of clouds in the MODIS satellite images, especially during winter. Cloud-free images representing the highest concentration of whiting events from each year were selected to compute the peak/maximum area covered by whiting and to determine the spatial distribution of whiting in the region. A total of 17 MODIS images (one image per year) were classified with the developed model. The extent of the areas covered by whiting were then computed, as shown in Table 6. The maximum coverage of whiting occurred in March 2012, followed by March 2003, whereas the minimum coverage of assessed whiting events was recorded in December 2010. The classification results were used to identify the common areas subjected to whiting. To statistically identify significant hot spots (High spatial frequency of whiting events overs 17 years), statistical analysis of spatial clustering was carried out using Optimized Hot Spot Analysis (Getis-Ord Gi*) [99,100]. This tool automatically aggregates whiting events and identifies statistically significant spatial clusters where the focus is on presence or absence of each whiting event rather than a measured attribute associated with whiting events. Figure 9 shows significant whiting spatiotemporal clusters, in the semi-enclosed gulf, with various levels of confidence, areas that are statistically significant at the 99 percent confidence level showed that whiting events were the frequent in the southwest sections of the Gulf and along the coasts of UAE, Qatar, Bahrain and opposite the coast of Al Jubail in Saudi Arabia.

Table 6. Cloud-free MODIS images that show peak whiting patches between 2002 and 2018 and the computed whiting area coverage.

| Year	Date	Whiting Area (km^2)	Percentage of Gulf Area
2002	5 February	15,655	6.55
2003	2 March	53,687	22.46
2004	9 February	29,874	12.50
2005	6 April	44,894	18.78
2006	30 January	30,549	12.78
2007	11 December	20,481	8.57
2008	22 February	47,887	20.04
2009	5 February	22,584	9.45
2010	16 December	12,100	5.06
2011	5 December	17,340	7.26
2012	4 March	60,847	25.46
2013	4 February	39,544	16.55
2014	10 November	15,137	6.33
2015	15 November	19,201	8.03
2016	10 February	30,480	12.75
2017	6 January	45,753	19.14
2018	3 February	22,159	9.27
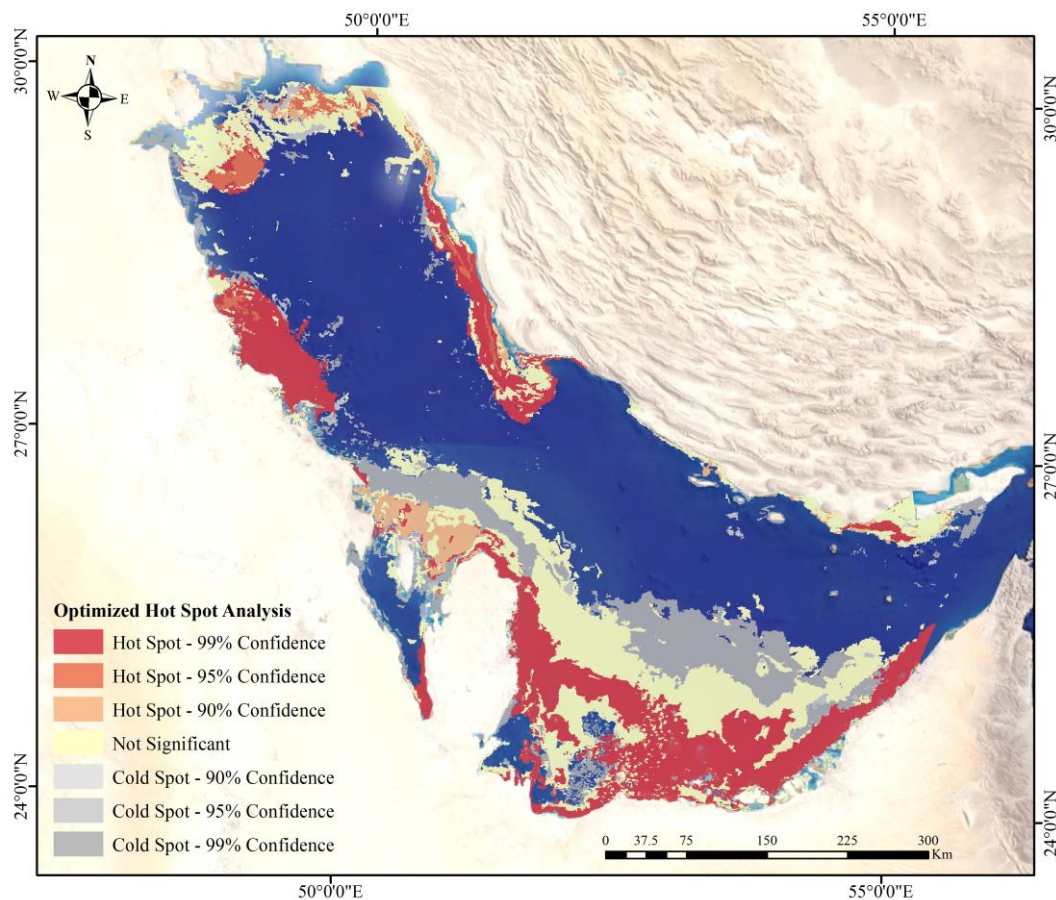
Figure 9. High spatial frequency of whiting events overs 17 years.

4. Conclusions

Previous studies mapping whiting events from satellite images, specifically in the Bahama Banks and in the coast of Southwest Florida, relied on the manual delineation of whiting on the basis of spatial contrast, spectral behaviour of whiting and derived spectral indices. Considering the limited studies on whiting event mapping in the Gulf, the present study aimed to document the spatial extent and the seasonal variability of whiting events in the Gulf between 2002 and 2018 using MODIS data. This study acquired and analysed extensive daily data for mapping and documenting, documented spatiotemporal distribution and presented an effective model (integrated CFS, Adaboost and rule-based classification) for detecting and classifying whiting in the Gulf using the MODIS data. The results of FS showed that the combination of the mean of the green band and the NDGB or the combination of the NDGB and CI were the most significant feature for detecting the brightness of in-water features compared with all the examined features in the classification. This study used various tree-based machine learning classifiers, namely, rule-based classification based on a single DT, GBDT, RF and AdaBoost, to classify the optimised multitemporal image objects. The results showed that the rule-based classification based on AdaBoost DT outperformed the supervised tree-based GEOBIA classifiers. Therefore, this study adopted the AdaBoost classification model to find a generic model for distinguishing objects of whiting water directly and classifying time series image objects by rule-based classification.

The adopted model showed an outstanding and expeditious approach to extracting and characterising whiting events quantitatively from time series images. Whiting events in the Gulf occurred during the winter season (November to March) and were extensively located in the southwestern section of the Gulf, mainly along the UAE coast. During the study period (2002–2018), the whiting events occurred exclusively for 5 to 34 days per year and covered areas ranging from 12,000 km^2 to 60,000 km^2. These events require further investigations for in-situ measurements and

laboratory analysis, on the basis of the common spatial distribution of whiting. Therefore, whiting in the Arabian Gulf merits further attention from the scientific community to examine biophysical, biogeochemical and environmental factors that may reveal the causes of the whiting occurrences.

References

1. Long, J.S.; Hu, C.; Robbins, L.L.; Byrne, R.H.; Paul, J.H.; Wolny, J.L. Optical and biochemical properties of a southwest Florida whiting event. *Estuar. Coast. Shelf Sci.* **2017**, *196*, 258–268. [CrossRef]

2. Morse, J.W.; He, S. Influence of T, S and PCO_2 on the homogeneous nucleation of calcium carbonate from seawater. Implications for whiting formation. *Mar. Chem.* **1993**, *41*, 291–298. [CrossRef]

3. Watkins, J.M.; Rudstam, L.G.; Crabtree, D.L.; Walsh, M.G. Is reduced benthic flux related to the Diporeia decline? Analysis of spring blooms and whiting events in Lake Ontario. *J. Great Lakes Res.* **2013**, *39*, 395–403. [CrossRef]

4. Thompson, J.B.; Schultze-Lam, S.; Beveridge, T.J.; Des Marais, D.J. Whiting events: Biogenic origin due to the photosynthetic activity of cyanobacterial picoplankton. *Limnol. Oceanogr.* **1997**, *42*, 133–141. [CrossRef] [PubMed]

5. Wurgaft, E.; Steiner, Z.; Luz, B.; Lazar, B. Evidence for Inorganic Precipitation of $CaCO_3$ on Suspended Solids in the Open Water of the Red Sea. *Mar. Chem.* **2016**, *186*, 145–155. [CrossRef]

6. Friedman, G.M. Biochemical and ultrastructural evidence for the origin of whitings: A biologically induced calcium carbonate precipitation mechanism: Comment and reply. *Geology* **1993**, *21*, 287–288. [CrossRef]

7. Bloch, R.; Littman, H.Z.; Elazari-Volcani, B. Occasional whiteness of the dead sea. *Nature* **1944**, *154*, 402–403. [CrossRef]

8. Bustos-Serrano, H.; Morse, J.W.; Millero, F.J. The formation of whitings on the Little Bahama Bank. *Mar. Chem.* **2009**, *113*, 1–8. [CrossRef]

9. Bathurst, R.G.C. *Carbonate Sediments and Their Diagenesis*, 2nd ed.; Developments in Sedimentology; Elsevier: Amsterdam, The Netherlands, 1975; Volume 12, p. 658.

10. Long, J.S.; Hu, C.; Wang, M. Long-term spatiotemporal variability of southwest Florida whiting events from MODIS observations. *Int. J. Remote Sens.* **2018**, *39*, 906–923. [CrossRef]

11. Robbins, L.L.; Blackwelder, P.L. Biochemical and ultrastructural evidence for the origin of whiting: A biologically induced calcium carbonate precipitation mechanism. *Geology* **1992**, *20*, 464–468. [CrossRef]

12. Dierssen, H.M.; Zimmerman, R.C.; Burdige, D.J. Optics and remote sensing of Bahamian carbonate sediment whitings and potential relationship to wind-driven Langmuir circulation. *Biogeosciences* **2009**, *6*, 487–500. [CrossRef]

13. Broecker, W.S.; Takahashi, T. Calcium carbonate precipitation on the Bahama Banks. *J. Geophys. Res.* **1966**, *71*, 1575–1602. [CrossRef]

14. Boss, S.K.; Neumann, A.C. Physical versus chemical processes of "whiting" formation in the Bahamas. *Carbonates Evaporites* **1993**, *8*, 135–148. [CrossRef]

15. Shinn, E.A.; Steinen, R.P.; Lidz, B.H.; Swart, P.K. Whitings, a Sedimentologic Dilemma. *J. Sediment. Petrol.* **1989**, *59*, 147–161. [CrossRef]

16. Cloud, P.E. Environment of Calcium Carbonate Deposition West of Andros Island Bahamas. *Geol. Surv. Prof. Pap.* **1962**, *350*, 170.

17. Riding, R.E.; Awramik, S.M. *Microbial Sediments*; Springer: Berlin, Germany, 2000; ISBN 978-3-642-08275-7.

18. Ohlendorf, C.; Sturm, M. Precipitation and Dissolution of Calcite in a Swiss High Alpine Lake. *Arctic Antarct. Alp. Res.* **2001**, *33*, 410–417. [CrossRef]

19. Otsuki, A.; Wetzel, R.G. Calcium and total alkalinity budgets and calcium carbonate precipitation of a small hard-water lake. *Arch. Hydrobiol.* **1974**, *73*, 14–30. [CrossRef]

20. Morse, J.W.; Gledhill, D.K.; Millero, F.J. CaCO$_3$ precipitation kinetics in waters from the Great Bahama Bank: Implications for the relationship between Bank hydrochemistry and whitings. *Geochim. Cosmochim. Acta* **2003**, *67*, 2819–2826. [CrossRef]

21. Shinn, E.A.; Kendall, C.G.S.C. Back to the Future. *Sediment. Rec.* **2011**, *9*, 4–9. [CrossRef]

22. Lidz, B.; Gibbons, H. Research on Whitings (Floating Patches of Calcium Carbonate Mud) Leads to Possible Explanation of Immense Middle East Oil Deposits. Available online: https://soundwaves.usgs.gov/2008/07/research.html (accessed on 30 September 2018).

23. Whitton, B.A. *Ecology of Cyanobacteria II: Their Diversity in Space and Time*; Springer: Dordrecht, The Netherlands, 2012; ISBN 978-94-007-3854-6.

24. Robbins, L.L.; Tao, Y.; Evans, C.A. Temporal and spatial distribution of whitings on Great Bahama Bank and a new lime mud budget. *Geology* **1997**, *25*, 947–950. [CrossRef]

25. Long, J.; Hu, C.; Robbins, L. Whiting events in SW Florida coastal waters: A case study using MODIS medium-resolution data. *Remote Sens. Lett.* **2014**, *5*, 539–547. [CrossRef]

26. Strong, A.E.; Eadie, B.J. Satellite observations of calcium carbonate precipitation in the Great Lakes. *Limnol. Ocean.* **1978**, *23*, 877–887. [CrossRef]

27. Heine, I.; Brauer, A.; Heim, B.; Itzerott, S.; Kasprzak, P.; Kienel, U.; Kleinschmit, B. Monitoring of calcite precipitation in hardwater lakes with multi-spectral remote sensing archives. *Water* **2017**, *9*, 15. [CrossRef]

28. Millero, J. The carbonate chemistry of grand bahama bank waters: After 18 years another look. *J. Geophys. Res.* **1984**, *89*, 3604–3614.

29. Long, J.S. Whiting Events Off Southwest Florida: Remote Sensing and Field Observations. Ph.D. Dissertation, University of South Florida, Tampa, FL, USA, 2016.

30. Lloyd, R.A. Remote Sensing of Whitings in the Bahamas. Master's Thesis, University of South Florida, Tampa, FL, USA, 2012.

31. Tao, Y. Whitings on the Great Bahama Bank: Distribution in Space and Time Using Space Shuttle Photographs. Ph.D. Dissertation, University of South Florida, Tampa, FL, USA, 1994.

32. Balch, W.M.; Gordon, H.R.; Bowler, B.C.; Drapeau, D.T.; Booth, E.S. Calcium carbonate measurements in the surface global ocean based on Moderate-Resolution Imaging Spectroradiometer data. *J. Geophys. Res. C Ocean.* **2005**, *110*, 1–21. [CrossRef]

33. Gordon, R.; Boynton, G.C.; Balch, W.M.; Harbour, D.S.; Smyth, T.J.; Bay, W.B. Retrieval of Coccolithophore from SeaWiFS Imagery Calcite Concentration radiance. *Geophys. Res. Lett.* **2001**, *28*, 1587–1590. [CrossRef]

34. Mitchell, C.; Hu, C.; Bowler, B.; Drapeau, D.; Balch, W.M. Estimating Particulate Inorganic Carbon Concentrations of the Global Ocean From Ocean Color Measurements Using a Reflectance Difference Approach. *J. Geophys. Res. Ocean.* **2017**, *122*, 8707–8720. [CrossRef]

35. Wells, A.J.; Illing, L.V. Present-day precipitation of calcium carbonate in the Persian Gulf. *Dev. Sedimentol.* **1964**, *1*, 429–435. [CrossRef]

36. Shanableh, A.; Imteaz, M.; Hamad, K.; Omar, M.; Merabtene, T.; Siddique, M. Potential impact of global warming on whiting in a semi-enclosed gulf. *Int. J. Glob. Warm.* **2017**, *13*, 411–425.

37. Shanableh, A.; Al-Ruzouq, R.; Al-Khayyat, G. Assessing the Spatial and Temporal Capacity of a Semi-Enclosed Gulf to Absorb and Release CO2 Using GIS and Remote Sensing. In Proceedings of the Global Civil Engineering Conference, Kuala Lumpur, Malaysia, 25–28 July 2017; pp. 1161–1173.

38. Sheppard, C.; Al-Husiani, M.; Al-Jamali, F.; Al-Yamani, F.; Baldwin, R.; Bishop, J.; Benzoni, F.; Dutrieux, E.; Dulvy, N.K.; Durvasula, S.R.V.; et al. *Environmental Concerns for the Future of Gulf Coral Reefs*; Springer: Dordrecht, The Netherlands, 2012; p. E1. ISBN 978-94-007-3007-6.

39. Kaempf, J.; Sadrinasab, M. The circualtion of the Persian Gulf: A numerical study. *Ocean Sci.* **2006**, *2*, 27–41, doi:10.5194/osd-2-129-2005.

40. Ben-Hasan, A.; Walters, C.; Christensen, V.; Al-Husaini, M.; Al-Foudari, H. Is reduced freshwater flow in Tigris-Euphrates rivers driving fish recruitment changes in the Northwestern Arabian Gulf? *Mar. Pollut. Bull.* **2018**, *129*, 1–7. [CrossRef] [PubMed]

41. Blaschke, T.; Hay, G.J.; Kelly, M.; Lang, S.; Hofmann, P.; Addink, E.; Queiroz Feitosa, R.; van der Meer, F.; van der Werff, H.; van Coillie, F.; et al. Geographic Object-Based Image Analysis—Towards a new paradigm. *ISPRS J. Photogramm. Remote Sens.* **2014**, *87*, 180–191. [CrossRef]

42. Makinde, E.O.; Salami, A.T.; Olaleye, J.B.; Okewusi, O.C. Object Based and Pixel Based Classification Using Rapideye Satellite Imager of ETI-OSA, Lagos, Nigeria. *Geoinform. FCE CTU* **2016**, *15*, 59. [CrossRef]

43. Petropoulos, G.P.; Vadrevu, K.P.; Kalaitzidis, C. Spectral angle mapper and object-based classification combined with hyperspectral remote sensing imagery for obtaining land use/cover mapping in a Mediterranean region. *Geocarto Int.* **2013**, *28*, 114–129. [CrossRef]

44. da Silva Junior, C.A.; Nanni, M.R.; de Oliveira-Júnior, J.F.; Cezar, E.; Teodoro, P.E.; Delgado, R.C.; Shiratsuchi, L.S.; Shakir, M.; Chicati, M.L. Object-based image analysis supported by data mining to discriminate large areas of soybean. *Int. J. Digit. Earth* **2019**, *12*, 270–292. [CrossRef]

45. Bisquert, M.; Bégué, A.; Deshayes, M. Object-based delineation of homogeneous landscape units at regional scale based on modis time series. *Int. J. Appl. Earth Obs. Geoinf.* **2015**, *37*, 72–82. [CrossRef]

46. Cano, E.; Denux, J.P.; Bisquert, M.; Hubert-Moy, L.; Chéret, V. Improved forest-cover mapping based on MODIS time series and landscape stratification. *Int. J. Remote Sens.* **2017**, *38*, 1865–1888. [CrossRef]

47. Vintrou, E.; Desbrosse, A.; Bégué, A.; Traoré, S.; Baron, C.; Lo Seen, D. Crop area mapping in West Africa using landscape stratification of MODIS time series and comparison with existing global land products. *Int. J. Appl. Earth Obs. Geoinf.* **2012**, *14*, 83–93. [CrossRef]

48. Bontemps, S.; Bogaert, P.; Titeux, N.; Defourny, P. An object-based change detection method accounting for temporal dependences in time series with medium to coarse spatial resolution. *Remote Sens. Environ.* **2008**, *112*, 3181–3191. [CrossRef]

49. Bisquert, M.; Bégué, A.; Deshayes, M.; Ducrot, D. Environmental evaluation of MODIS-derived land units. *GISci. Remote Sens.* **2017**, *54*, 64–77. [CrossRef]

50. Bellón, B.; Bégué, A.; Lo Seen, D.; de Almeida, C.A.; Simões, M. A remote sensing approach for regional-scale mapping of agricultural land-use systems based on NDVI time series. *Remote Sens.* **2017**, *9*, 600. [CrossRef]

51. Kim, M.; Madden, M.; Warner, T.T. Forest Type Mapping using Object-specific Texture Measures from Multispectral Ikonos Imagery: Segmentation Quality and Image Classification Issues. *Photogramm. Eng. Remote Sens.* **2009**, *75*, 819–829. [CrossRef]

52. Baatz, M.; Sch, A. Multiresolution Segmentation: An optimization approach for high quality multi-scale image segmentation. *J. Photogramm. Remote Sens.* **2004**, *58*, 239–258.

53. Grybas, H.; Melendy, L.; Congalton, R.G. A comparison of unsupervised segmentation parameter optimization approaches using moderate- and high-resolution imagery. *GISci. Remote Sens.* **2017**, *54*, 515–533. [CrossRef]

54. Kim, M.; Warner, T.A.; Madden, M.; Atkinson, D.S. Multi-scale GEOBIA with very high spatial resolution digital aerial imagery: Scale, texture and image objects. *Int. J. Remote Sens.* **2011**, *32*, 2825–2850. [CrossRef]

55. Hussain, M.; Chen, D.; Cheng, A.; Wei, H.; Stanley, D. Change detection from remotely sensed images: From pixel-based to object-based approaches. *ISPRS J. Photogramm. Remote Sens.* **2013**, *80*, 91–106. [CrossRef]

56. Gao, Y.; Mas, J.F.; Kerle, N.; Pacheco, J.A.N. Optimal region growing segmentation and its effect on classification accuracy. *Int. J. Remote Sens.* **2011**, *32*, 3747–3763. [CrossRef]

57. Johnson, B.; Bragais, M.; Endo, I.; Magcale-Macandog, D.; Macandog, P. Image Segmentation Parameter Optimization Considering Within- and Between-Segment Heterogeneity at Multiple Scale Levels: Test Case for Mapping Residential Areas Using Landsat Imagery. *ISPRS Int. J. Geo-Inf.* **2015**, *4*, 2292–2305. [CrossRef]

58. Drăguţ, L.; Csillik, O.; Eisank, C.; Tiede, D. Automated parameterisation for multi-scale image segmentation on multiple layers. *ISPRS J. Photogramm. Remote Sens.* **2014**, *88*, 119–127. [CrossRef]

59. Zhang, X.; Xiao, P.; Feng, X. An unsupervised evaluation method for remotely sensed imagery segmentation. *IEEE Geosci. Remote Sens. Lett.* **2012**, *9*, 156–160. [CrossRef]

60. Espindola, G.M.; Camara, G.; Reis, I.A.; Bins, L.S.; Monteiro, A.M. Parameter selection for region-growing image segmentation algorithms using spatial autocorrelation. *Int. J. Remote Sens.* **2006**, *27*, 3035–3040. [CrossRef]

61. Laliberte, A.S.; Browning, D.M.; Rango, A. A comparison of three feature selection methods for object-based classification of sub-decimeter resolution UltraCam-L imagery. *Int. J. Appl. Earth Obs. Geoinf.* **2012**, *15*, 70–78. [CrossRef]

62. Ma, L.; Cheng, L.; Li, M.; Liu, Y.; Ma, X. Training set size, scale, and features in Geographic Object-Based Image Analysis of very high resolution unmanned aerial vehicle imagery. *ISPRS J. Photogramm. Remote Sens.* **2015**. [CrossRef]

63. Al-Ruzouq, R.; Shanableh, A.; Barakat, A.; Gibril, M.; AL-Mansoori, S. Image Segmentation Parameter Selection and Ant Colony Optimization for Date Palm Tree Detection and Mapping from Very-High-Spatial-Resolution Aerial Imagery. *Remote Sens.* **2018**, *10*, 1413. [CrossRef]

64. Georganos, S.; Grippa, T.; Vanhuysse, S.; Lennert, M.; Shimoni, M.; Kalogirou, S.; Wolff, E. Less is more: Optimizing classification performance through feature selection in a very-high-resolution remote sensing object-based urban application. *GISci. Remote Sens.* **2018**, *55*, 221–242. [CrossRef]

65. Zhou, Y.; Chen, Y.; Feng, L.; Zhang, X.; Shen, Z.; Zhou, X. Supervised and Adaptive Feature Weighting for Object-Based Classification on Satellite Images. *IEEE J. Sel. Top. Appl. Earth Obs. Remote Sens.* **2018**, *11*, 3224–3234. [CrossRef]

66. Benediktsson, J.A.; Pesaresi, M.; Arnason, K. Classification and feature extraction for remote sensing images from urban areas based on morphological transformations. *IEEE Trans. Geosci. Remote Sens.* **2003**, *41*, 1940–1949. [CrossRef]

67. Dash, M.; Liu, H. Feature selection for classification. *Intell. Data Anal.* **1997**, *1*, 131–156. [CrossRef]

68. Löw, F.; Michel, U.; Dech, S.; Conrad, C. Impact of feature selection on the accuracy and spatial uncertainty of per-field crop classification using Support Vector Machines. *ISPRS J. Photogramm. Remote Sens.* **2013**, *85*, 102–119. [CrossRef]

69. Guyon, I.; Elisseeff, A. An introduction to variable and feature selection. *J. Mach. Learn. Res.* **2003**, *3*, 1157–1182.

70. Duro, D.C.; Franklin, S.E.; Dubé, M.G. Multi-scale object-based image analysis and feature selection of multi-sensor earth observation imagery using random forests. *Int. J. Remote Sens.* **2012**, *33*, 4502–4526. [CrossRef]

71. Hu, M.; Wu, F. Filter-wrapper hybrid method on feature selection. In Proceedings of the 2010 Second WRI Global Congress on Intelligent Systems, Wuhan, China, 16–17 December 2010; pp. 98–101. [CrossRef]

72. Ma, L.; Fu, T.; Blaschke, T.; Li, M.; Tiede, D.; Zhou, Z.; Ma, X.; Chen, D. Evaluation of Feature Selection Methods for Object-Based Land Cover Mapping of Unmanned Aerial Vehicle Imagery Using Random Forest and Support Vector Machine Classifiers. *ISPRS Int. J. Geo-Inf.* **2017**, *6*, 51. [CrossRef]

73. Gumus, E.; Kirci, P. Selection of spectral features for land cover type classification. *Expert Syst. Appl.* **2018**, *102*, 27–35. [CrossRef]

74. Hamedianfar, A.; Barakat, A.M. Gibril Large-scale urban mapping using integrated geographic object-based image analysis and artificial bee colony optimization from worldview-3 data. *Int. J. Remote Sens.* **2019**. [CrossRef]

75. Ridha, M.; Pradhan, B. Catena An improved algorithm for identifying shallow and deep-seated landslides in dense tropical forest from airborne laser scanning data. *Catena* **2018**, *167*, 147–159. [CrossRef]

76. Hall, M.A.; Smith, L.A. Feature subset selection: A correlation based filter approach. In *International Conference on Neural Information Processing and Intelligent Information Systems*; Springer: Berlin, Germany, 1997; pp. 855–858.

77. Hall, M.A. Correlation-based feature selection of discrete and numeric class machine learning. In Proceedings of the 17th International Conference on Machine Learning, San Francisco, CA, USA, 29 June–2 July 2000; pp. 359–366.

78. Hall, M.A.; Smith, L.A. Practical feature subset selection for machine learning. In Proceedings of the 21st Australasian Computer Science Conference ACSC'98, Perth, Australia, 4–6 February 1998; Volume 98, pp. 181–191.

79. Hall, M.A.; Holmes, G. Benchmarking Attribute Selection Techniques for Discrete Class Data Mining. *IEEE Trans. Knowl. Data Eng.* **2003**, *15*, 1437–1447. [CrossRef]

80. Trimble, T. *ECognition Developer 8.7 Reference Book*; Trimble Germany GmbH: Munich, Germany, 2011; pp. 319–328.

81. Curran, P. Multispectral remote sensing of vegetation amount. *Prog. Phys. Geogr.* **1980**, *4*, 315–341. [CrossRef]

82. Mcfeeters, S.K. The use of the Normalized Difference Water Index (NDWI) in the delineation of open water features. *Int. J. Remote Sens.* **1996**, *17*, 1425–1432. [CrossRef]

83. Xu, H. Modification of normalised difference water index (NDWI) to enhance open water features in remotely sensed imagery. *Int. J. Remote Sens.* **2006**, *27*, 3025–3033. [CrossRef]

84. Hu, C. A novel ocean color index to detect floating algae in the global oceans. *Remote Sens. Environ.* **2009**, *113*, 2118–2129. [CrossRef]

85. Hu, C.; Lee, Z.; Franz, B. Chlorophyll a algorithms for oligotrophic oceans: A novel approach based on three-band reflectance difference. *J. Geophys. Res. Ocean.* **2012**, *117*, 1–25. [CrossRef]

86. Xue, K.; Zhang, Y.; Duan, H.; Ma, R.; Loiselle, S.; Zhang, M. A remote sensing approach to estimate vertical profile classes of phytoplankton in a Eutrophic lake. *Remote Sens.* **2015**, *7*, 14403–14427. [CrossRef]

87. Fensholt, R.; Sandholt, I. Derivation of a shortwave infrared water stress index from MODIS near- and shortwave infrared data in a semiarid environment. *Remote Sens. Environ.* **2003**, *87*, 111–121. [CrossRef]

88. Jordan, C.F. Derivation of Leaf-Area Index from Quality of Light on the Forest Floor. *Ecology* **1969**, *50*, 663–666. [CrossRef]

89. Huete, A.; Didan, K.; Miura, T.; Rodriguez, E.P.; Gao, X.; Ferreira, L.G. Overview of the radiometric and biophysical performance of the MODIS vegetation indices. *Remote Sens. Environ.* **2002**, *83*, 195–213. [CrossRef]

90. Tucker, C.J. Red and photographic infrared linear combinations for monitoring vegetation. *Remote Sens. Environ.* **1979**, *8*, 127–150. [CrossRef]

91. Zarco-Tejada, P.J.; Berjón, A.; López-Lozano, R.; Miller, J.R.; Martín, P.; Cachorro, V.; González, M.R.; De Frutos, A. Assessing vineyard condition with hyperspectral indices: Leaf and canopy reflectance simulation in a row-structured discontinuous canopy. *Remote Sens. Environ.* **2005**, *99*, 271–287. [CrossRef]

92. Freund, Y.; Schapire, R.E. A Decision-Theoretic Generalization of On-Line Learning and an Application to Boosting. *J. Comput. Syst. Sci.* **1997**, *55*, 119–139. [CrossRef]

93. Friedl, M.A.; McIver, D.K.; Hodges, J.C.F.; Zhang, X.Y.; Muchoney, D.; Strahler, A.H.; Woodcock, C.E.; Gopal, S.; Schneider, A.; Cooper, A.; et al. Global land cover mapping from MODIS: Algorithms and early results. *Remote Sens. Environ.* **2002**, *83*, 287–302. [CrossRef]

94. DeFries, R. Multiple Criteria for Evaluating Machine Learning Algorithms for Land Cover Classification from Satellite Data. *Remote Sens. Environ.* **2000**, *74*, 503–515. [CrossRef]

95. Zhou, Z.; Huang, J.; Wang, J.; Zhang, K.; Kuang, Z.; Zhong, S.; Song, X. Object-oriented classification of sugarcane using time-series middle-resolution remote sensing data based on AdaBoost. *PLoS ONE* **2015**, *10*, e0142069. [CrossRef] [PubMed]

96. Maxwell, A.E.; Warner, T.A.; Fang, F. Implementation of machine-learning classification in remote sensing: An applied review. *Int. J. Remote Sens.* **2018**, *39*, 2784–2817. [CrossRef]

97. Congalton, R.G.; Green, K. *Assessing the Accuracy of Remotely Sensed Data: Principles and Practices*, 2nd ed.; CRC Press, Taylor & Francis Group: Boca Raton, FL, USA, 2009; p. 183, ISBN 978-1-4200-5512-2.

98. Xu, L.; Yan, P.; Chang, T. Best first strategy for feature selection. In Proceedings of the 9th International Conference on Pattern Recognition, Rome, Italy, 14 May–17 November 1988; pp. 706–708.

99. Cheng, Z.; Zu, Z.; Lu, J. Traffic crash evolution characteristic analysis and spatiotemporal hotspot identification of urban road intersections. *Sustainability* **2018**, *11*, 161. [CrossRef]

100. Al-Ruzouq, R.; Hamad, K.; Abu Dabous, S.; Zeiada, W.; Khalil, M.A.; Voigt, T. Weighted Multi-attribute Framework to Identify Freeway Incident Hot Spots in a Spatiotemporal Context. *Arab. J. Sci. Eng.* **2019**. [CrossRef]